PERGAMON

International Journal of Heat and Mass Transfer 44 (2001) 4009–4026

International Journal of HEAT and MASS TRANSFER

www.elsevier.com/locate/ijhmt

New-wall modeling for complex flows using the large eddy simulation technique in curvilinear coordinates

Y.A. Hassan *, H.R. Barsamian

Department of Nuclear Engineering, Texas A&M University, College Station, TX 77843-3133, USA

Received 8 August 2000; received in revised form 9 January 2001

Abstract

This investigation presents modifications and improvements to the dynamic subgrid scale model and introduces a new-wall model. These modifications are implemented in the large eddy simulation technique in curvilinear coordinates. They are then validated and tested in three-dimensional complex geometries. The large eddy simulation method captures many scales of turbulence up to the grid size. A closure model is used to simulate subgrid turbulence. The Smagorinsky and dynamic subgrid models are presented and tested. The dynamic model overcomes many of the deficiencies of the Smagorinsky subgrid scale model. Spatial and temporal low-pass filters have been introduced in the dynamic subgrid scale model for numerical stability. Several near-wall models are considered for the large eddy simulation technique. A local averaging technique lends these models to be applicable in complex geometry situations. A new model is introduced which overcomes planar averaging near the wall and captures ejection and sweep effects. These models have been implemented in a large eddy simulation computer program. Results are validated and tested in a lid driven cavity flow at Reynolds number of 10 000. A single tube in a channel is simulated to show the applicability of the models to complex geometries with attachment and separation as well as end-wall effects. The shedding effect was captured and turbulence statistical characteristics were acceptable.

1. Introduction

Not all computational fluid dynamic (CFD) methods are applicable to solve turbulence problems, much less in complex geometries. As in any engineering method, a compromise is needed between accuracy of results and time/cost of effort in acquiring the results. Resolving all the scales of a turbulent flow is too costly, while employing highly empirical turbulence models to complex problems could give inaccurate simulation results. The large eddy simulation method would achieve the above requirements. Here, the large scales in the flow are solved and the small scales are modeled. The Smagorinsky [31] model is commonly used to describe the eddy viscosity. Germano et al. [8] have introduced the dynamic procedure for better prediction of the eddy viscosity. Lilly [19] proposed modifications to the dynamic model of [8] based on a least-square minimization method.

A characteristic of turbulent flows is the high gradients near solid walls. The viscosity of a fluid enforces the no-slip condition and acts as a 'sink' for momentum [32], leading to a characteristic length near the wall that is viscosity dominated. The difference in length scales between the near-wall and rest of the flow necessitates the treatment of the surface layer separately from the rest of the flow. The logarithmic region (or inertial sublayer) is the link between the different scales. There are many models that relate the shear stress at the wall to a location within the logarithmic region. However, most models do not make a distinction for the direction of the shear stress at the wall. Since turbulent flows are three-dimensional, this approximation may not be a good one, especially for complex flows with separation. It should be noted that it is possible to resolve the wall layer in a CFD calculation. However, a large amount of resources must be allocated for this purpose. For

* Corresponding author. Tel.: +1-979-845-7090; fax: +1-979-845-6443.

E-mail address: y-hassan@tamu.edu (Y.A. Hassan).

0017-9310/01/$ - see front matter
PII: S0017-9310(01)00047-3

engineering applications one may consider wall models as a compromise between accuracy and available resources.

In the following investigation, the large eddy simulation method is used in complex geometries. Several wall models are considered for these simulations. Section 2 gives a brief description of the large eddy simulation technique with applicable subgrid scale models. Then, several wall models are discussed including a newly developed model. Simulations are performed in a lid-driven cavity and a single tube in a channel as test cases for the models in complex geometries.

2. Large eddy simulation

Large eddy simulation (LES) uses a spatial filtering operation to separate the large scales that are to be calculated from the small scales that are to be modeled [18]. A one dimensional filtered variable in LES is defined as

$$\overline{f}(x,t) = \int \overline{G}(x,x')f(x',t)\,\mathrm{d}x', \tag{1}$$

where $\overline{G}(x,x')$ represents a low-pass spatial filter function with a characteristic width Δ. A filter operator is normalized to one. Filter functions that are common to LES include the box filter or the tophat filter in real space, the Gaussian filter in real or wave space, and the sharp Fourier cutoff filter in wave space.

Applying the filtering operation to the continuity and momentum equations and using the commutation properties, filtered equations are obtained.

$$\frac{\partial \overline{u}_i}{\partial x_i} = 0, \tag{2}$$

$$\frac{\partial \overline{u}_i}{\partial t} + \frac{\partial \overline{u}_i\overline{u}_j}{\partial x_j} = -\frac{1}{\rho}\frac{\partial \overline{p}}{\partial x_i} + \nu\frac{\partial^2 \overline{u}_i}{\partial x_j \partial x_j} - \frac{\partial \tau_{ij}}{\partial x_j}, \tag{3}$$

where the subgrid scale (SGS) stress tensor τ_{ij} must be expressed as a function of resolved flow variables.

In the Smagorinsky model, proportionality between the anisotropic part of the SGS stresses and the large-scale strain rate tensor is assumed

$$\tau_{ij} - \frac{1}{3}\delta_{ij}\tau_{kk} = -2\nu_{\mathrm{T}}\overline{S}_{ij}, \tag{4}$$

where ν_{T} is the SGS eddy viscosity and is generally assumed to be a scalar quantity, and $\overline{S}_{ij}$ is the large-scale strain rate tensor. The following definition applies for the SGS eddy viscosity

$$\nu_{\mathrm{T}} = (C_{\mathrm{S}}\Delta)^2|\overline{S}|, \tag{5}$$

where the local strain rate is defined by

$$|\overline{S}| = (2\overline{S}_{ij}\overline{S}_{ij})^{1/2}, \tag{6}$$

$$\overline{S}_{ij} = \frac{1}{2}\left(\frac{\partial \overline{u}_i}{\partial x_j} + \frac{\partial \overline{u}_j}{\partial x_i}\right) \tag{7}$$

and C_{S} is the model parameter ranging from about 0.065 to 0.25, and Δ is the length scale used in the definition of the filter.

The dynamic subgrid scale (DSGS) model has shown to predict SGS stresses better than the Smagorinsky eddy viscosity model [1,9,24,35]. However, the DSGS itself has several drawbacks that include the necessity of planar averaging and bounds on the model coefficient [8]. In complex geometry situations where no homogeneous direction exists, planar averaging of the model coefficient, as suggested by Gremano et al. [8], is not practical. Dynamic models have been used where upper and lower bounds on the model coefficient are applied to avoid large variations that may lead to instabilities [2]. In addition to these strong variations in space, the model coefficient contains a significant fraction of negative values as observed by [20,21]. Smoothing of C locally or truncation efforts are mathematically inconsistent; however, there is a tradeoff between these and numerical instabilities as observed when no smoothing or averaging of any form is done. Breuer and Rodi [4] have suggested a lowpass filtering of the dynamic coefficient. While this approach keeps C time dependent, it only allows variations with low frequencies. They suggested using a recursive lowpass digital filter given by

$$C^{n+1}_{\mathrm{filtered}} = (1-\varepsilon)C^n + \varepsilon C^{n+1} \tag{8}$$

with values of ε on the order of 10^{-3}. Here, the damping of the high frequency oscillations in time are extended to space as well. The absence of a homogeneous direction in complex flows and the need for numerical stability necessitates such a move. A spatial low pass filter is applied on the model coefficient on the level of the test filter. While local averaging does overcome the absence of a homogeneous direction, it does not filter out the high frequency oscillations. On the other hand, a low pass filter of the test filter volume performs the necessary high frequency damping to help with numerical stability of the solver. One must be careful since time averaging of the coefficient causes the model to lose Galilean invariance. Meneveau et al. [22] found that a mismatch of timescales between the real backscattering events and the modeled ones based in the resolved scales is the main reason of backscattering instability in numerical simulations. They suggest the use of a Langrangian time-averaging as remedy.

3. Wall modeling

To avoid the placement of a large number of grid points near a wall, a wall model is generally used to capture near-wall effects. These models are empirical

boundary conditions that bridge the gap in the wall region. Although this issue receives less attention than SGS modeling for LES, it is as important.

One must be careful when using these models, since most wall models are developed by simplifying assumptions and tested in simple flows. These models are not easily applicable to cases involving streamwise and spanwise surface curvatures, pressure gradients, and separation as in complex geometries. The most popular approximate boundary conditions used in large eddy simulation are shear stress boundary condition in the streamwise and spanwise directions with a zero velocity in the wall normal direction that are designed to be consistent with the logarithmic law-of-the-wall in the mean.

In laminar flows, the linear relationship between the wall shear stress and velocity enables a simplified method of capturing wall effects

$$\tau_{\mathrm{w}} = \mu \frac{\partial u_{\mathrm{P}}}{\partial y}\bigg|_{\mathrm{w}}, \tag{9}$$

where τ_{w} is the wall shear stress, μ is the viscosity, y is the normal distance of the first grid point from the wall, and u is the velocity at that point (P) relative to the wall. However, in a turbulent flow, this relationship is no longer linear.

In turbulent flows, there exists a region that exhibits well-established features including a logarithmic section. This a priori known feature is used to estimate the near-wall velocity that obeys the well-known logarithmic law-of-the-wall

$$u^+ = y^+ \quad \text{for } y^+ < 11.81, \tag{10}$$

$$u^+ = \frac{\langle u_{\mathrm{P}} \rangle}{u_\tau} = 2.5 \log\left(\frac{u_\tau y}{\nu}\right) + 5.2, \tag{11}$$

where y^+ and u^+ are defined as

$$y^+ \equiv \frac{\rho y u_\tau}{\mu}, \tag{12}$$

$$u^+ = \frac{u}{u_\tau}. \tag{13}$$

The friction velocity, u_τ, is defined as

$$u_\tau = \sqrt{\frac{\tau_{\mathrm{w}}}{\rho}}. \tag{14}$$

It is stipulated that for the LES method, models with distinct terms for the wall shear stress components are more appropriate. The advantage is that the first grid point can be specified in the logarithmic region $30 < y^+ < 200$. There will be no need to resolve the wall layer. New approaches in the application of these models were necessary to accommodate for complex geometries. Modifications were also performed to enhance the ability of a model to simulate more complex physics. The following sections will give detailed descriptions of these wall models.

4. The Schumann model with Grotzbach's modifications

Schumann's [30] model applied to large eddy simulation uses the shear stress boundary conditions in the tangential directions coupled with a zero velocity condition in the wall normal direction

$$\tau_{\mathrm{ub}} = u_{\mathrm{P}} \frac{\langle \tau_{\mathrm{ub}} \rangle}{\langle u_{\mathrm{P}} \rangle}, \tag{15}$$

$$\tau_{\mathrm{wb}} = \mu \frac{w_{\mathrm{P}}}{y}, \tag{16}$$

$$v_{\mathrm{P}} = 0.0, \tag{17}$$

where τ_{ub} and τ_{wb} are the streamwise and spanwise wall shear stresses, and $\langle \cdot \rangle$ represents ensemble averaging. The ratio of the averages in Eq. (15) forms an empirical constant that could be obtained through experimental means for certain flow types. This requirement of a priori knowledge of the mean shear stress near the wall led to modifications of the model.

Grotzbach [10] used a different approach to evaluate $\langle u_{\mathrm{P}} \rangle$. He took the mean velocity near the wall from the time average of his integration and then used the logarithmic velocity profile of Eq. (11) to calculate the wall shear stress. Hence a priori knowledge of the wall shear was not necessary.

5. The shifted and ejection models

Piomelli et al. [25] went even further by taking into account the elongated structures present near the wall. From observations, he formulated his model according to the fact that the local wall shear stress is related not to the local near-wall 'parallel' velocity but to the near-wall velocity at a location shifted downstream by an optimal streamwise displacement. His shifted boundary conditions are given by:

$$\tau_{\mathrm{ub}} = u_{\mathrm{P}+\Delta s} \frac{\langle \tau_{\mathrm{ub}} \rangle}{\langle u_{\mathrm{P}} \rangle}, \tag{18}$$

$$\tau_{\mathrm{wb}} = w_{\mathrm{P}+\Delta s} \frac{\langle \tau_{\mathrm{ub}} \rangle}{\langle w_{\mathrm{P}} \rangle}, \tag{19}$$

$$v_{\mathrm{P}} = 0.0, \tag{20}$$

where Δs is a shift in the streamwise flow direction and has been shown through experimental means to be $y\tan(8^\circ)$ for $30 < y^+ < 50$–60 and equal to $y\tan(13^\circ)$

for larger distances. This quantity represents the shift in the correlation between velocity and wall stress. This is known as the shifted model [25].

Piomelli et al. [25] also made a suggestion to consider the ejection model observed in experiments. This model is conceptually based on the dynamical processes known to occur in near-wall turbulence. The 'bursts' are termed as ejection and sweep depending on the direction of vertical motion. They significantly affect the wall stress. The ejection model notes that significant turbulent stress countering events involve vertical motion, so the vertical component of the velocity rather than the horizontal should be correlated with the wall shear stress. The model takes into account the fact that the correlation is negative, hence the proposal that the streamwise wall shear stress should correlate negatively with the wall normal velocity at the estimation point. The ejection model is given by

$$\tau_{\mathrm{ub}} = \langle \tau_{\mathrm{ub}} \rangle - C\rho u_\tau v_{\mathrm{P}+\Delta s}, \tag{21}$$

$$\tau_{\mathrm{wb}} = w_{\mathrm{P}+\Delta s} \frac{\langle \tau_{\mathrm{ub}} \rangle}{\langle w_{\mathrm{P}} \rangle}, \tag{22}$$

$$v_{\mathrm{P}} = 0.0, \tag{23}$$

where C is a constant of order 1 and the wall shear is obtained by solving iteratively a generalized law-of-the-wall.

6. Werner and Wengle model

The model introduced by Werner and Wengle [33] is considered next. They have introduced a wall model based on the linear law-of-the-wall and the power law description of the form $u^+ = A(y^+)^B$ (with $A = 8.3$ and $B = 1/7$). The model for evaluating the streamwise shear stresses is given by

$$|\tau_{\mathrm{ub}}| = \frac{2\mu|u_{\mathrm{P}}|}{\Delta y} \quad \text{for } |u_{\mathrm{P}}| \leqslant \frac{\mu}{2\rho\Delta y} A^{2/(1-B)}, \tag{24}$$

$$|\tau_{\mathrm{ub}}| = \rho \left[\frac{1-B}{2} A^{[(1+B)/(1-B)]} \left(\frac{\mu}{\rho\Delta y} \right)^{1+B} + \frac{1+B}{A} \times \left(\frac{\mu}{\rho\Delta y} \right)^{B} |u_{\mathrm{P}}| \right]^{2/(1+B)} \quad \text{for } |u_{\mathrm{P}}| > \frac{\mu}{2\rho\Delta y} A^{2/(1-B)}. \tag{25}$$

This approach assumes that the instantaneous tangential velocity component inside the first cell is in phase with the instantaneous wall shear stress. This procedure offers the advantages that no average values are required, numerical problems in reattachment regions are avoided, and no iteration method is necessary to determine the wall shear stress because it can be obtained analytically [4].

7. Model modifications

In complex geometries it is difficult to obtain a distinct homogeneous plane. For LES wall models that require the calculation of the mean shear stress, this is an added difficulty. A new approach is used to overcome this difficulty. It is stipulated that as long as the grid curvature change in a region of the complex geometry does not change with a high rate, the given section may be used for evaluation of the mean shear in that region. However, implementation of this method will encounter difficulties when deciding the limits of the curvature change. A local averaging technique is suggested instead. With the local averaging technique, the planar neighboring points of a wall grid are used to evaluate $\langle u_{\mathrm{P}} \rangle$ and Eq. (11) used to evaluate $\langle \tau_{\mathrm{ub}} \rangle$. This process not only overcomes the difficulty of distinguishing a homogeneous plane, but also enables consideration of direction shifts in the near-wall velocity. However, if the wall cells are too small, the divergence from the mean velocity value will no longer satisfy the law-of-the-wall in the mean.

Again, let us consider the current view of the turbulent boundary layer. Through flow visualizations, Kline et al. [13] have shown an organized trend among the elongated streaks in the region very close to the wall. Streaks containing lower momentum fluid were observed to rise slowly, and break up in a process termed 'bursting'. As mentioned above, ejections are interpreted as the movement of low momentum fluid away from the wall. Sweep on the other hand represents the motion of high momentum fluid towards the wall. Ejections and sweeps are common in the buffer region between the linear sublayer and the logarithmic region of the mean velocity profile [29]. Since the 'bursting' phenomena and the presence of a shift in the correlation between velocity and wall stress may significantly alter the wall shear stress, the physical models introduced by Piomelli et al. [25] are implemented in the model derived by Werner and Wengle [33]. The new streamwise shear stress is given by

$$|\tau_{\mathrm{ub}}| = \frac{2\mu|u_{\mathrm{P}}|}{\Delta y} \quad \text{for } |u_{\mathrm{P}}| \leqslant \frac{\mu}{2\rho\Delta y} A^{2/(1-B)}, \tag{26}$$

$$|\tau_{\mathrm{ub}}| = \rho \left[\frac{1-B}{2} A^{[(1+B)/(1-B)]} \left(\frac{\mu}{\rho\Delta y} \right)^{1+B} + \frac{1+B}{A} \times \left(\frac{\mu}{\rho\Delta y} \right)^{B} |u_{\mathrm{P}+\Delta s}| \right]^{2/(1+B)} - C\rho u_\tau v_{\mathrm{P}+\Delta s} \quad \text{for } |u_{\mathrm{P}}| > \frac{\mu}{2\rho\Delta y} A^{2/(1-B)}. \tag{27}$$

The new model uses a shifted near-wall velocity value at a downstream location for the streamwise and spanwise shear stresses. Also, a 'correction' is made to the wall

shear stress in the streamwise direction to account for the 'bursting' phenomena observed by the addition of the term introduced by Piomelli et al. [25]. This new model is implemented in a large eddy simulation code.

8. Computer program

A large eddy simulation technique is used in a curvilinear coordinate formulation with the new-wall models. The computer program GUSTCC is a multi-dimensional finite volume computer program designed to solve the conservation equations of continuity and momentum for a general incompressible fluid [5]. The limitations of the computer program include single-phase isothermal flow conditions with no other force fields except for gravity. A fixed grid in a single domain is also required.

GUSTCC uses a staggered grid formulation to discretize the governing equations. The method uses different control volumes for the mass and momentum variables. Control volumes in GUSTCC are in general non-orthogonal curvilinear coordinates. Although these cells are irregular in shape and size, they are structured.

The solution of GUSTCC is second-order accurate in space and time. It uses the central differencing scheme for spatial discretization and the Crank–Nicolson scheme for temporal discretization. The equations of flow are solved using the covariant projections as the dependent variables. This necessitates the calculation of contravariant components that are constructed when needed to calculate fluxes by using local values of the metric coefficient and the tensor transformation rules. There is no additional storage required. For turbulent flows, the viscosity represents the turbulent viscosity and is calculated using the appropriate SGS model. Internal structures use the blockage concept given by Patankar [23].

9. Lid-driven cavity simulation

A large eddy simulation of the three-dimensional lid-driven cavity flow was performed. The lid-driven cavity is a widely used simulation tool for testing numerical schemes and physical models. Its simple geometry and well-defined flow structures make the cavity flow an attractive test case. For isothermal flows, visualization of flow structures in a lid-driven cavity delineates interestingly complex phenomena. For the following investigation, the purpose is twofold. One is to show the ability of GUSTCC to correctly capture the complex flow structures using LES calculations. The other is to compare several of the wall models described above to available experimental data. Comparison between the Smagorinsky and modified dynamic SGS closure models is also performed.

In previous experiments, it has been observed that for Reynolds numbers below 5000, the flow is essentially laminar [14,26]. As the Reynolds number is increased, the flow observes a transition region between Reynolds numbers of 6000 and 8000 becoming more turbulent near the walls and at a Reynolds number of 10 000, the flow near the downstream eddy becomes fully turbulent [14]. We have considered the case corresponding to $Re = 10\,000$. This is a challenging test case for wall models and turbulence closure because the flow experiences large separated regimes displaying laminar, transitional and turbulent physics.

Fig. 1 gives the basic flow features of a lid-driven cavity indicating the secondary recirculation in the x–y plane near the lower downstream wall and upper and lower upstream wall. In the y–z plane, pairs of Taylor–Gortler-like (TGL) vortices and lower corner vortices are shown. The mechanism causing the TGL vortices is the inherent instability of the concave free shear layer that separates the primary vortex from the downstream secondary eddy (DSE). These vortices become distorted at the higher Reynolds numbers because the onset of turbulence occurs within the adjacent downstream free shear layer [15]. The spiraling features in the direction of flow are, however, evident. The corner vortex, the DSE and TGL vortices are all integrally inter-related. Koseff and Street [14] showed that the size of the DSE is strongly influenced by the characteristics of the corner vortex. From an overall viewpoint, the high degree of non-uniformity in the flow structures causes unsteadiness in the cavity [12].

The computational grid ($32 \times 32 \times 32$) is uniform in the spanwise direction, but non-uniform in the streamwise and transverse directions. The computation was carried out on the entire domain at all times, with rigid no-slip wall boundaries on all sides except for the top plane, which had a constant wall velocity of U_B (where B is the cavity length). Physical dimensions of 0.01 m in each direction were used, implying a spanwise aspect ratio (SAR) of 1:1. A lid velocity of 1.0 m/s was enforced. The grid in the x–y plane is shown in Fig. 2. The working fluid is water.

Some early three-dimensional numerical simulations of lid-driven cavity flows have been performed by [6,7], where comparisons of flow structures were made with experimental observations. Quantitative results were not in good agreement. [12,35] have performed simulations primarily focusing on the applicability of the dynamic closure model through quantitative verification of comparisons to experimental measurements in terms of the Reynolds stress quantities, time-dependent flow characteristics and energy spectra. In the present work, similar comparisons are made. The focus of the investigation is the LES application and performance evaluation of the

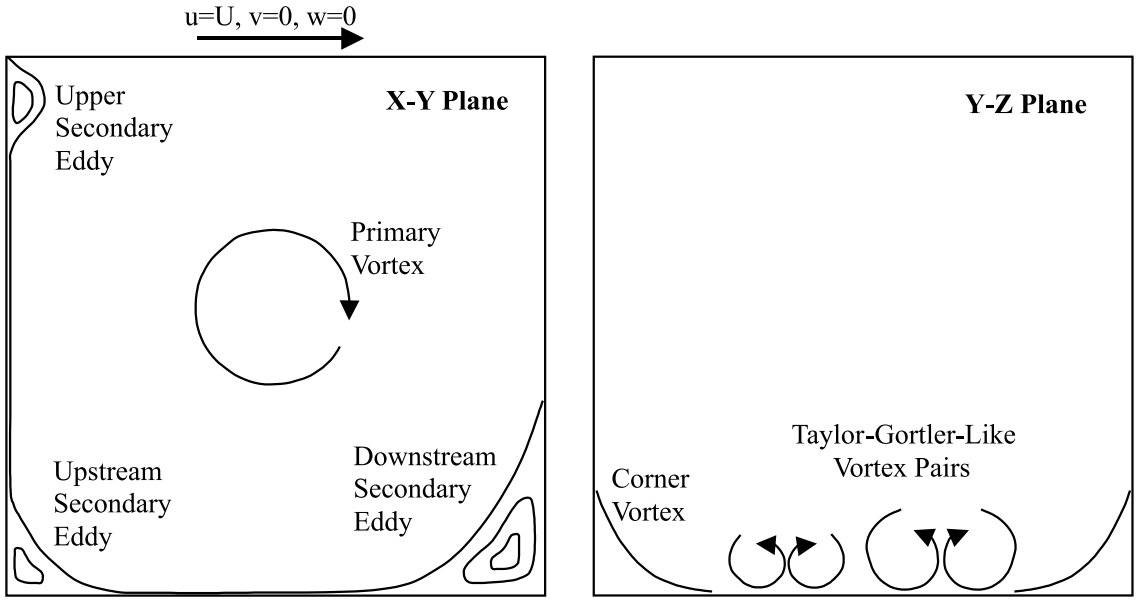

Fig. 1. Basic flow features of shear driven cavity flow.

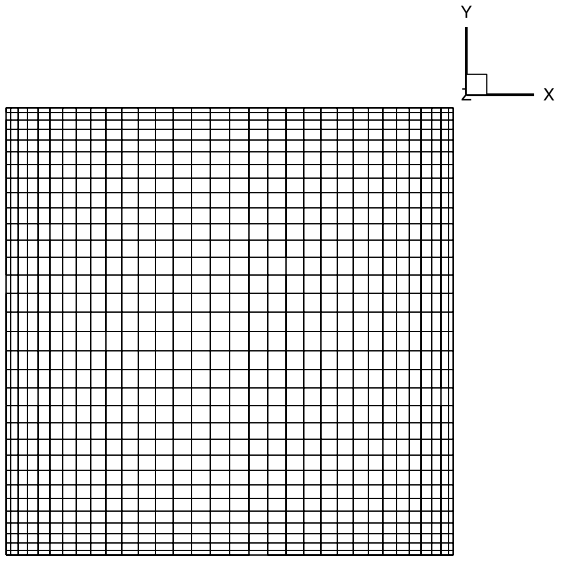

Fig. 2. Lid-driven cavity numerical grid in x–y plane.

different wall models under the complex deterministic flow. The LES results are first compared to experimental evidence thereby verifying the validity of the models.

Given the Reynolds number based on the lid velocity, U_B, and the cavity length, B, it is possible to estimate the Kolomogorov and Taylor length scales in the flow. The Kolomogorov length scale was evaluated to be $\sim 1 \times 10^{-5}$ m while the Taylor microscale was $\sim 5 \times 10^{-4}$ m. The maximum grid size in the domain is $\Delta = 0.0004$ m which is 1.25 times less than the Taylor microscale. This satisfied the minimum required grid resolution. Also, distances in non-dimensional wall units were evaluated. A maximum value of 50 was calculated for the boundary control volumes and 200 for the bulk of the flow. These satisfy the recommendations given by [24]. A constant time step of $\sim 1 \times 10^{-4}$ s was used to advance the flow calculation. While a minimum required time step size of $\sim 1 \times 10^{-3}$ s is necessary. The Courant number CFL was $0.333 < 1.0$ for the simulations.

Results are compared with experimental data of [26]. Two sets of simulations were performed. One used different wall models while the other used different closure models. The wall models include the Schumann model, the shifted model and the Werner and Wengle model. The modifications discussed above were applied. The ejection model was rejected due to numerical stability problems. The second set of simulations used the SGS closure models of Smagorinsky and dynamic procedure.

Results will be given in the form of mean velocities $\overline{u}/U_B$ and $\overline{v}/U_B$, root-mean-square (rms) velocities $\sqrt{\langle u''^2 \rangle}/U_B$ and $\sqrt{\langle v''^2 \rangle}/U_B$, and Reynolds stresses $\langle u''v'' \rangle / U_B^2$ on the respective centerlines in the midplane of the test case. All values are normalized with respect to the lid-driven velocity U_B.

All wall models herein are the modified models, but we will use the original author name given to the models for brevity. The following set of LES simulations used the Smagorinsky closure model. Considering mean velocity values at the midplane centerlines, Fig. 3 shows

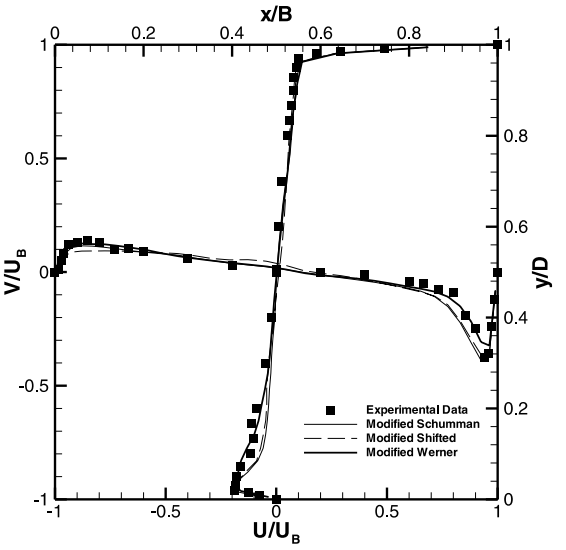

Fig. 3. Mean velocity profiles of lid-driven cavity at midplane centerline using different wall models.

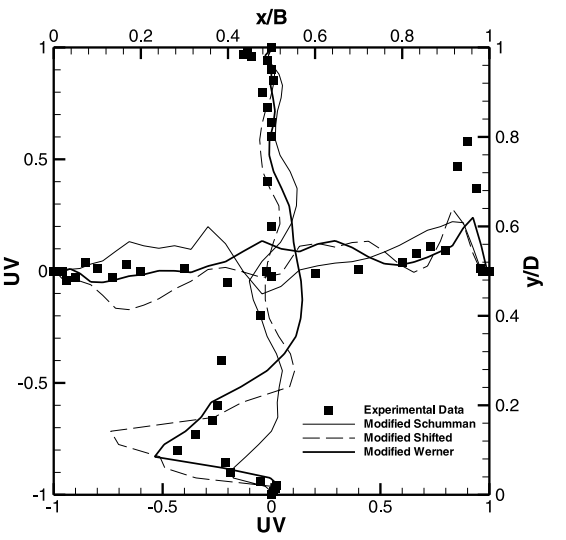

Fig. 5. Reynolds stress profiles of lid-driven cavity at midplane centerline using different wall models.

good comparison among the models tested and the experimental data. All models cover the wall region accurately by observing the correct slope. The Werner model, although slightly underpredicting the downstream maximum value, has very good agreement with both the peak values and width of the boundary layers at each end. The Schumann and sifted models underpredict the boundary layer width near the bottom and upstream walls.

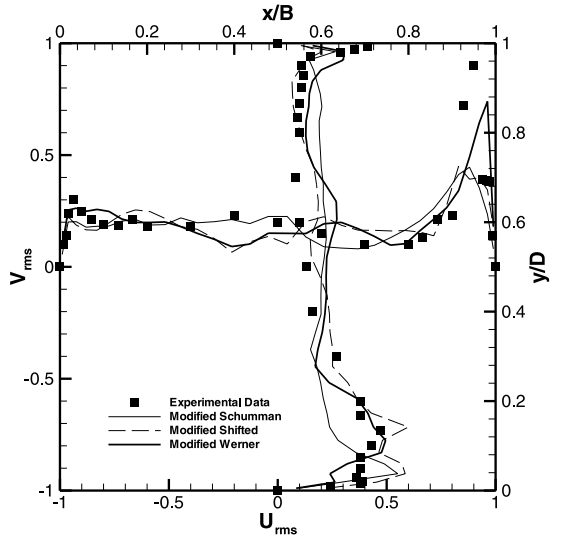

Fig. 4. Root-mean-square value profiles of lid-driven cavity at midplane centerline using different wall models.

Fig. 4 shows the rms velocities for the same test cases. Two notables about the Werner model include good maximum value agreement at the downstream wall and capture of the 'zigzag' phenomena of the boundary layer near the bottom wall (although the magnitude is underpredicted). The other two models do not perform as well in these two regions. Some discrepancies are observed in the bulk region. This could be due to the error propagation from the wall to the central region where grid resolution is coarser.

Agreement with the more complex Reynolds stresses in not very good in terms of capturing the boundary layer maximum values as seen in Fig. 5. From these observations, it may be stated that accuracy of wall models in complex geometries is substantially decreased as compared to channel type flows for which most models are tested.

Although there was no significant differences among the tested models, the Werner model overall fared better compared to the experimental data. All showed very good agreement in their mean quantities, but some discrepancies were observed in the root-mean-square velocity and Reynolds stress values. In subsequent simulations, the Werner wall model is deemed satisfactory and used accordingly.

The second study involved a comparison between the Smagorinsky and modified dynamic SGS closure models. Considering the same physical dimensions, results using a computational grid of $(50 \times 50 \times 32)$ cells are also shown. As stated, only the Werner wall model is applied. Using the same set of conditions for the above simulations, the mean values at the midplane centerline are shown in Fig. 6. No advantage of one model over the

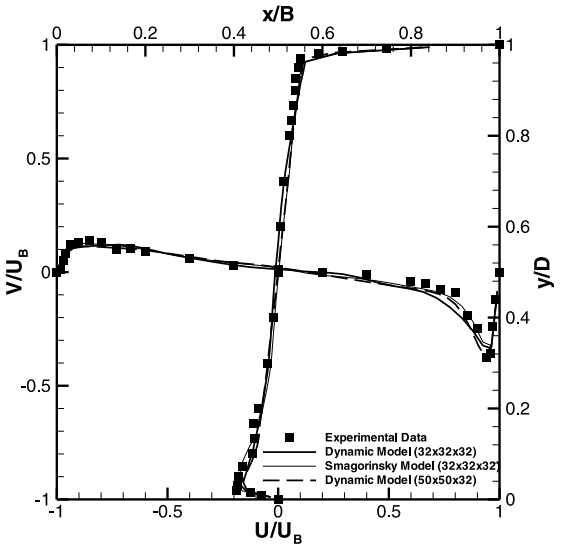

Fig. 6. Mean velocity profiles of lid-driven cavity at midplane centerline using different SGS closure models.

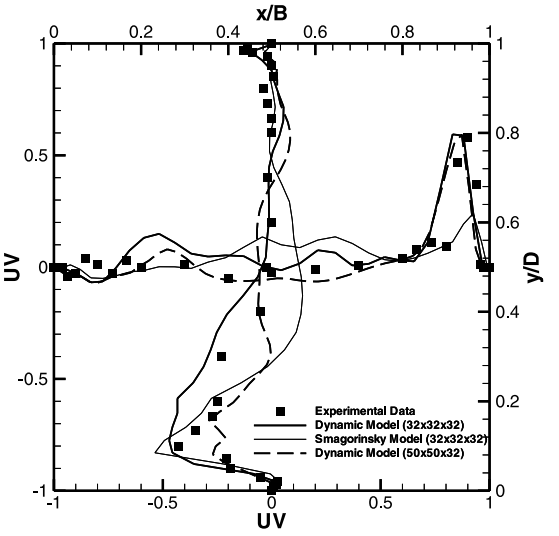

Fig. 8. Reynolds stress profiles of lid-driven cavity at midplane centerline using different SGS closure models.

other is seen in the mean quantities as well as the rms values shown in Fig. 7. However, as Fig. 8 delineates, the Reynolds stresses of the dynamic SGS model are substantially in better agreement with experimental data than the Smagorinsky model. This is clear in the downstream wall where the dynamic model captures the maximum value accurately as for the bottom and top walls. From these results it may be concluded that although differences in mean quantities are negligible between the Smagorinsky and dynamic models, the

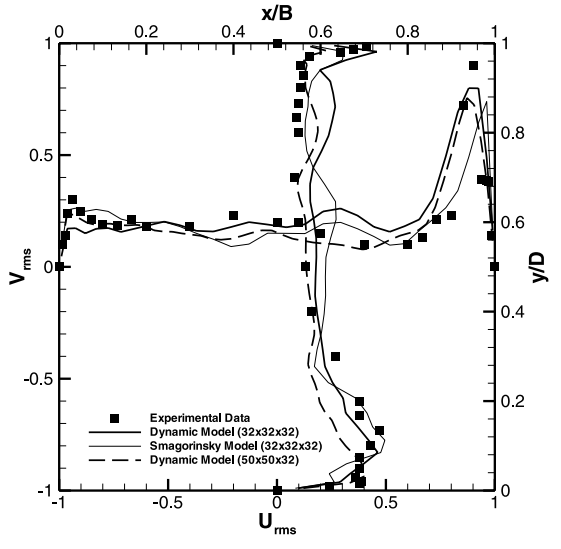

Fig. 7. Root-mean-square values of lid-driven cavity at midplane centerline using different SGS closure models.

Reynolds stresses are somewhat better predicted using the dynamic procedure where a local filtering procedure of the model coefficient was used and is applicable to complex flow geometries. Considering the case with large number of control volumes, there is no significant difference between the smaller case indicating satisfactory grid resolution for the simulations performed with $(32 \times 32 \times 32)$ the cells.

Section 10 describes some of the flow structures captured by the LES calculations. Similar characteristics were found among all the models tested. Therefore, observations only from a single simulation case are presented.

Fig. 9 delineate the instantaneous velocity vector field of the lid-driven cavity at the x–y midplane. The top of the lid is moving from left to right at the prescribed velocity U_B. The main circulation cell near the cavity center is clearly seen. The vectors clearly reveal the downstream and upstream secondary eddies in the recirculating flow. Shifting of these zones is observed as well.

In a similar form, the velocity vectors at a location near the downstream wall are plotted in the y–z plane. The x-direction vorticity contours are also overlain in Fig. 10. Counter rotation is indicated by the dashed contours. Three pairs of TGL vortices and corner vortices are visible. The presence of TGL vortices precludes the possibility that the flow will be two-dimensional. The corner vortex originates from the adjustment of the shear and pressure forces acting on the recirculating fluid to the no-slip condition imposed by the presence of the end-wall. These visualizations of TGL and corner vortices and the transitional behavior agree with the

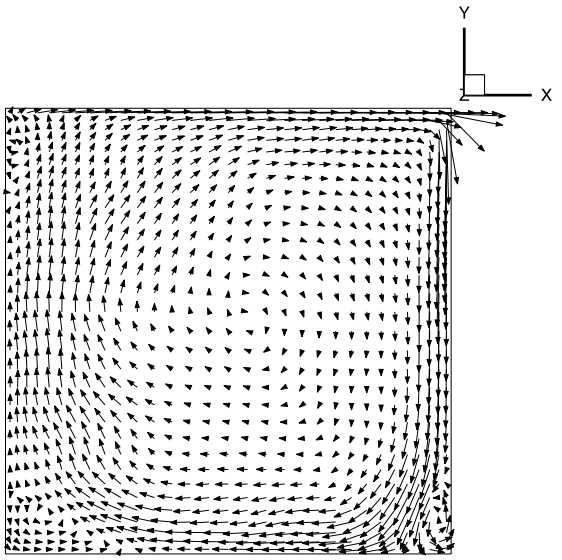

Fig. 9. Instantaneous velocity vectors at x–y midplane.

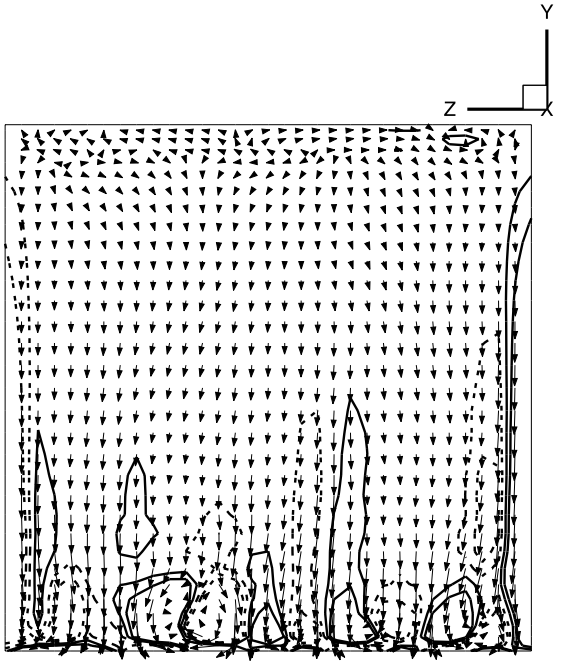

Fig. 10. Instantaneous velocity vectors near downstream wall and x-direction vorticity contours.

observations of [15]. It should be noted that the highest level of turbulence intensity occurs near the DSE region and upper half of the downstream wall, which is again consistent with experiments.

Three-dimensional flow structures are plotted in Fig. 11. While the lid is moving in the positive x-direction on the upper wall, the vorticity isosurface at a value of −75 Hz are plotted. It is seen that the vorticity is created on the top plane due to the large shear and transported by large-scale structures throughout the cavity. Again, circulation near the downstream wall show the transitional behavior of TGL vortices. These structures are coupled with the primary recirculating flow.

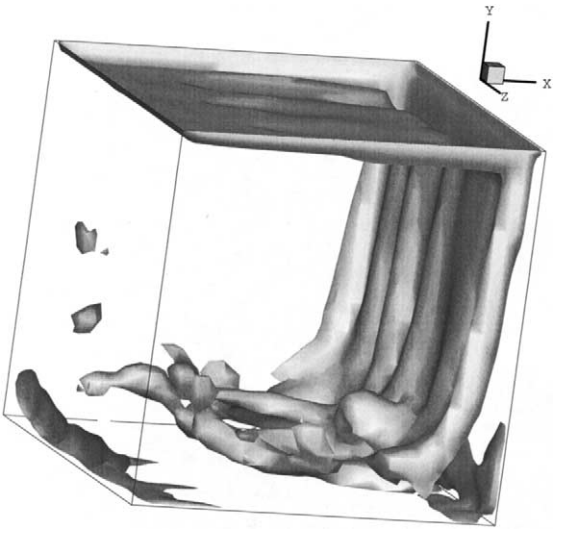

Fig. 11. Z-vorticity isosurface of lid-driven cavity.

These observations show the ability of the computer program GUSTCC to accurately capture complex physical phenomena in a transitional flow. Additional complex structures involving internal structures known as bluff bodies are considered in the next two sections.

10. Single tube simulation

In the above section the modified Werner and Wengle wall model and the modified dynamic SGS closure model were shown to behave well in LES of a lid-driven cavity. Here, these models are used in a LES calculation for a flow past a bluff body.

Study of bluff body flows is of direct engineering significance. The physical phenomena that are inherent to bluff body flows may lead to structural failure. Therefore, understanding the unsteady behavior and flow structures is of great importance. Some of the physical phenomena include separation with partial reattachment, unsteady vortex shedding, high turbulence levels and large-scale turbulent structures which contribute to the mass and momentum transport [27].

Here, the LES approach is implemented using the GUSTCC computer program to capture the unsteady

flow behind a circular cylinder in a narrow channel. In general, vortex structures behind a circular cylinder extend several diameter lengths downstream. These are known as Karman vortex streets [34]. Although at very low Reynolds numbers, the flow is two-dimensional, complex three-dimensional structures begin to appear above Reynolds values of 150 [11] and therefore, three-dimensional simulations are essential.

As the Reynolds number increases, the flow behind a circular cylinder has been classified to have different identifiable characteristics. These are well described by [34]. For the purpose of our calculation, the Reynolds number based on the freestream velocity and cylinder diameter is 21 700. This is defined to be in the subcritical range where the wake characteristics remain relatively similar [17]. It should be noted that in the following investigation, the cylinder is placed in a narrow channel. Roshko [28] found that vortex-shedding characteristics are changed when a plate is brought closer to the cylinder. He observed a decrease in shedding frequency and the vortex formation region was wider and longer.

The purpose of our calculations is twofold. First, qualitative observations of flow characteristics behind a circular cylinder in a channel are described and compared to similar experimental visualizations. Second, sensitivity studies of the GUSTCC computer program for complex geometries are performed. These include the effect of the SGS model, grid resolution and temporal resolution.

A schematic of the simulation geometry in the x–y plane is shown in Fig. 12. Expected patterns of vortex structures are sketched in the figure delineating the alternating eddying motion. For a given tube diameter D, an inlet section of length $2D$ was used to implement the boundaries and develop the flow. Here, small fluctuations were added to the mean inlet profile. The region in the cylinder wake extended for a distance of over $6D$. A spanwise distance of $5D$ was used. The width of the channel was $P = 31.8$ mm and the diameter of the cylinder $D = 21.7$ mm. Fig. 13 shows the $95 \times 38 \times 32$ curvilinear grid used for the simulation. Non-uniform grids were concentrated around the cylinder. Here, the positive x-direction has streamwise flow. In the z-direction, the grids are concentrated near the boundary walls.

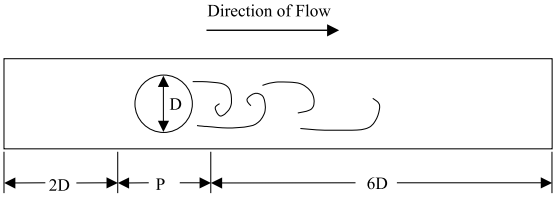

Fig. 12. Schematic of single tube in a channel.

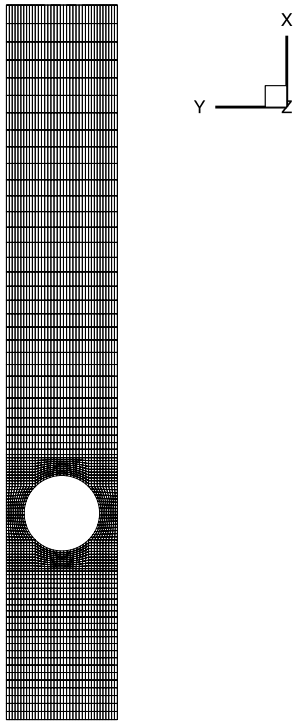

Fig. 13. Single tube nodalization.

The instantaneous velocity magnitude and cross-flow velocity for a single shedding cycle are shown first. Figs. 14 and 15 give contours of four frames for the normalized velocity magnitude and cross-flow velocity at the simulation x–y midplane, respectively. Each frame is 0.01 s apart. The figures represent a full shedding cycle ($\sim$25) Hz. The normalized velocity magnitudes show the highest flow to occur in the passage between the wall and the tube. These high velocities are then combined in the wake of the tube near the center of the channel. The lowest velocities are observed in between this region and the tube wall. Alternating low and high velocity magnitude wavelike structures are also observed near the channel walls. These structures are carried downstream. Cross-flow velocities represent the occurrences of highest transverse flow in the structure. The shedding behavior of the flow produces the high cross-flow values at a frequency consistent with the shedding of vortices behind the tube.

Figs. 16 and 17 delineate the transverse velocity isosurface depicting positive and negative contours for two frames. The alternating regions of positive (violet) and negative (green) flow velocity of 0.2 m/s correspond to Karman vortices [16]. There is a decrease in the strength of shedding amplitude with increased distance from the tube. The wake of the flow at this Reynolds number is clearly three-dimensional. The shedding velocities have consistent structures near the center of the spanwise

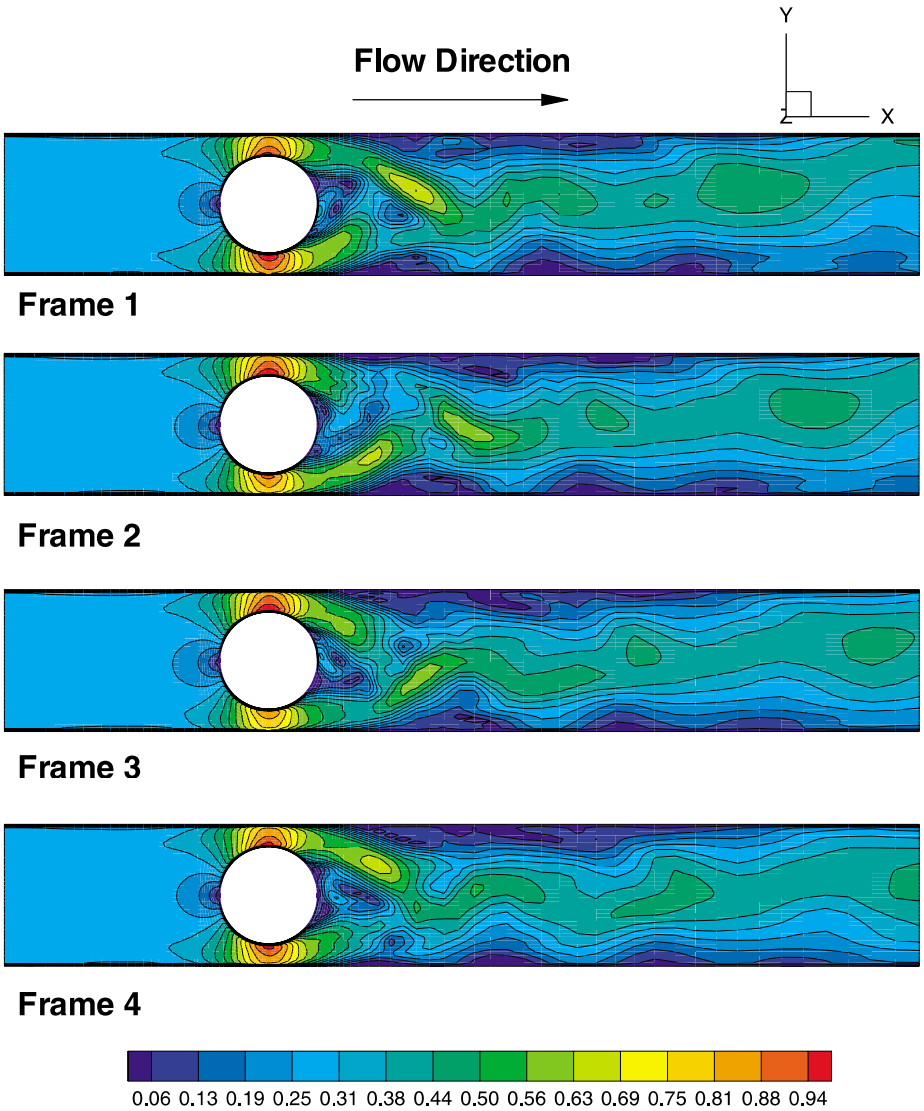

Fig. 14. Normalized velocity magnitude of single tube in a channel for four sequential frames.

direction, while the structure of shedding is not so apparent near the top and bottom walls.

Contours of instantaneous z-vorticity for the same cycles at the flow midplane are shown in Fig. 18 (units are in Hz). The alternating motion of the two shear layers separating from the cylinder sides is observed. These shear layers cause instabilities in the flow leading to the development of the Karman vortex street. An unsteady recirculation region is observed that alternates from one edge of the wall to the other and encompasses a range of large and small structures. In an unobstructed bluff body, where channel walls are absent, the flow structures tend to increase in size with increasing streamwise distance [16]. However, due to the proximity of the walls, the large structures are kept at relatively constant integral lengths and, as observed by [28], encounter a shift in shedding frequency. Although somewhat weaker than the shedding vortices, rotational structures are present near the walls indicating the wavelike structures mentioned above to be recirculation zones that propagate downstream with alternating cycles in sync with the shedding frequency.

While in laminar flows, periodic transverse fluctuations are observed, in turbulent flows, low-frequency intermittent velocity fluctuations are present [34]. The non-dimensional instantaneous values shown in Fig. 19(a) and (b) agree with the above statement. In Fig. 19(a), the streamwise instantaneous velocity values are

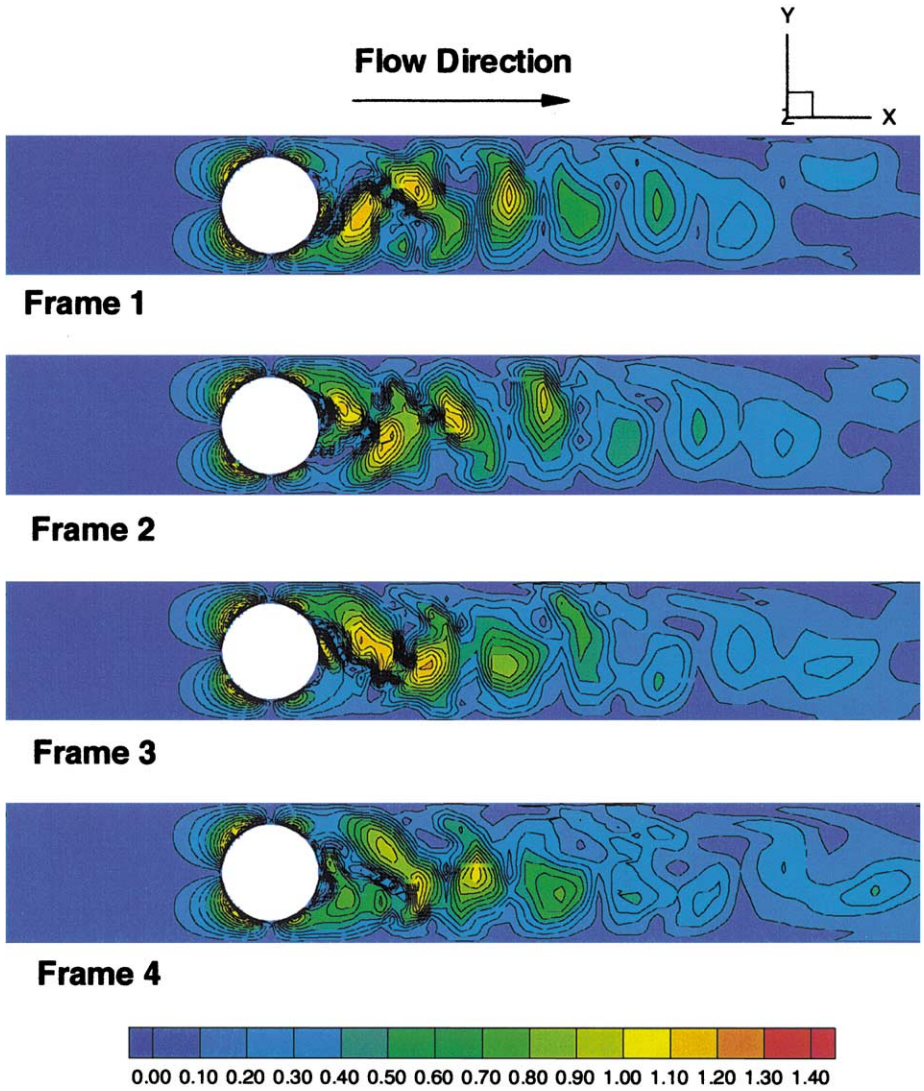

Fig. 15. Cross flow velocity magnitude of single tube in a channel for four sequential frames.

plotted as a function of time step at $x/D = 0.65$, 0.81. Both positions are within the recirculation zone of the tube wake and are generally negative except for a short time. Fig. 19(b) shows the instantaneous transverse velocity at the same locations. Some form of periodic behavior is apparent among the low-frequency fluctuations. The fluctuating frequencies are higher for the streamwise values relative to the transverse velocities. This will become clear in PSD plots below.

The spectra of velocities are considered next. The non-dimensional PSD of streamwise and transverse velocities are plotted as a function of frequency in Fig. 20(a) and (b) for the centerline $x/D = 0.65$ at the midplane and near the wall. The plots use 1024 samples for the FFT. The inertial subrange covers about a decade in frequency. The $-5/3$ slope is also shown in the plots. Although not very sharp, a peak is observed in Fig. 20(b) for the midplane PSD. This corresponds to the shedding frequency or Strouhal frequency. On the other hand a smaller peak at twice this frequency is seen for the streamwise velocity PSD near the midplane. These are due to the instantaneous velocity distributions in the tube wake shown above. The values located near the walls do not show a similar trend.

The non-dimensional streamwise mean velocity value at the midplane centerline is plotted as a function of non-dimensional position in Fig. 21(a). The statistics were accumulated only for four shedding cycles. In the downstream region, there is a decrease in velocity. This is due to the end wall effects. Fig. 21(b)–(d) show

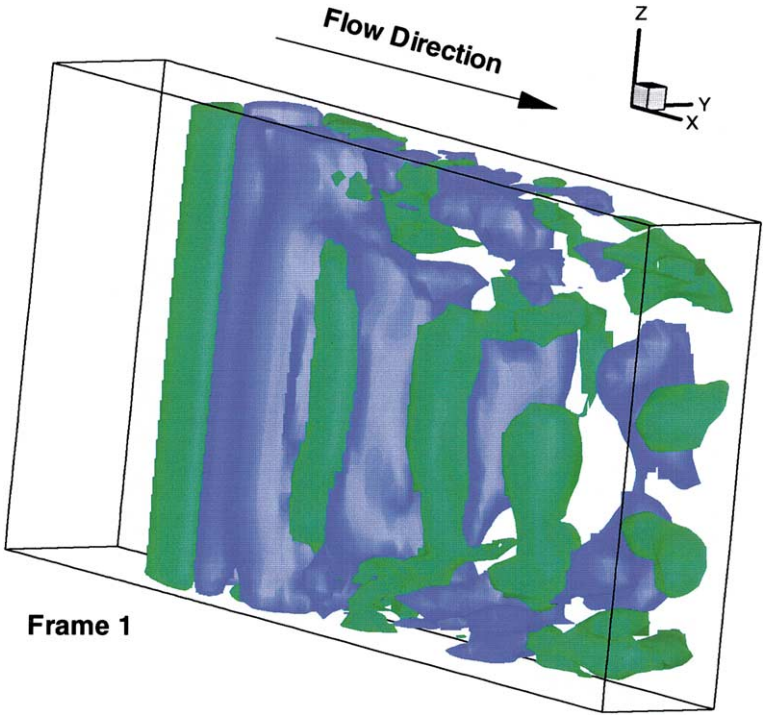

Fig. 16. Transverse velocity isosurface contours at positive and negative value of 0.2 for single tube for frame 1.

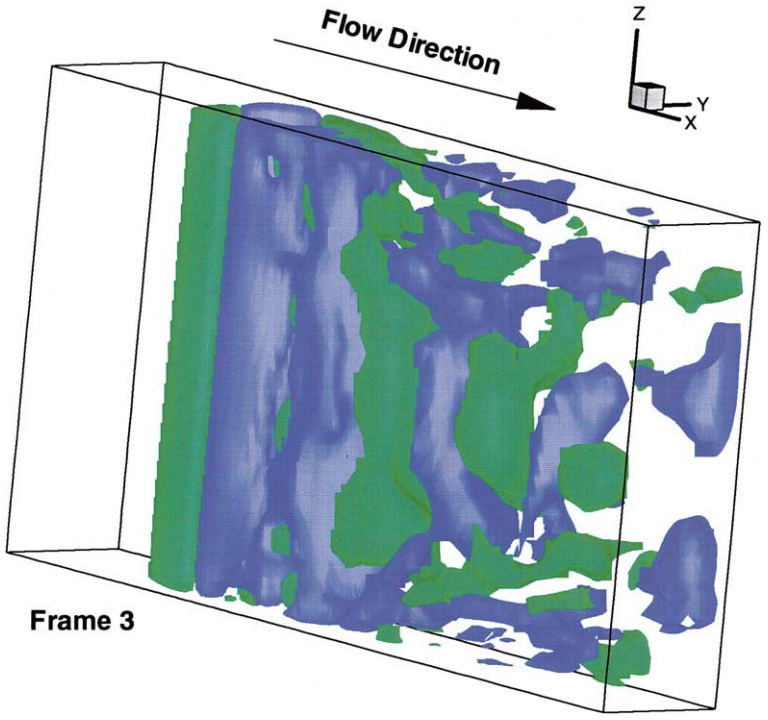

Fig. 17. Transverse velocity isosurface contours at positive and negative value of 0.2 for single tube for frame 3.

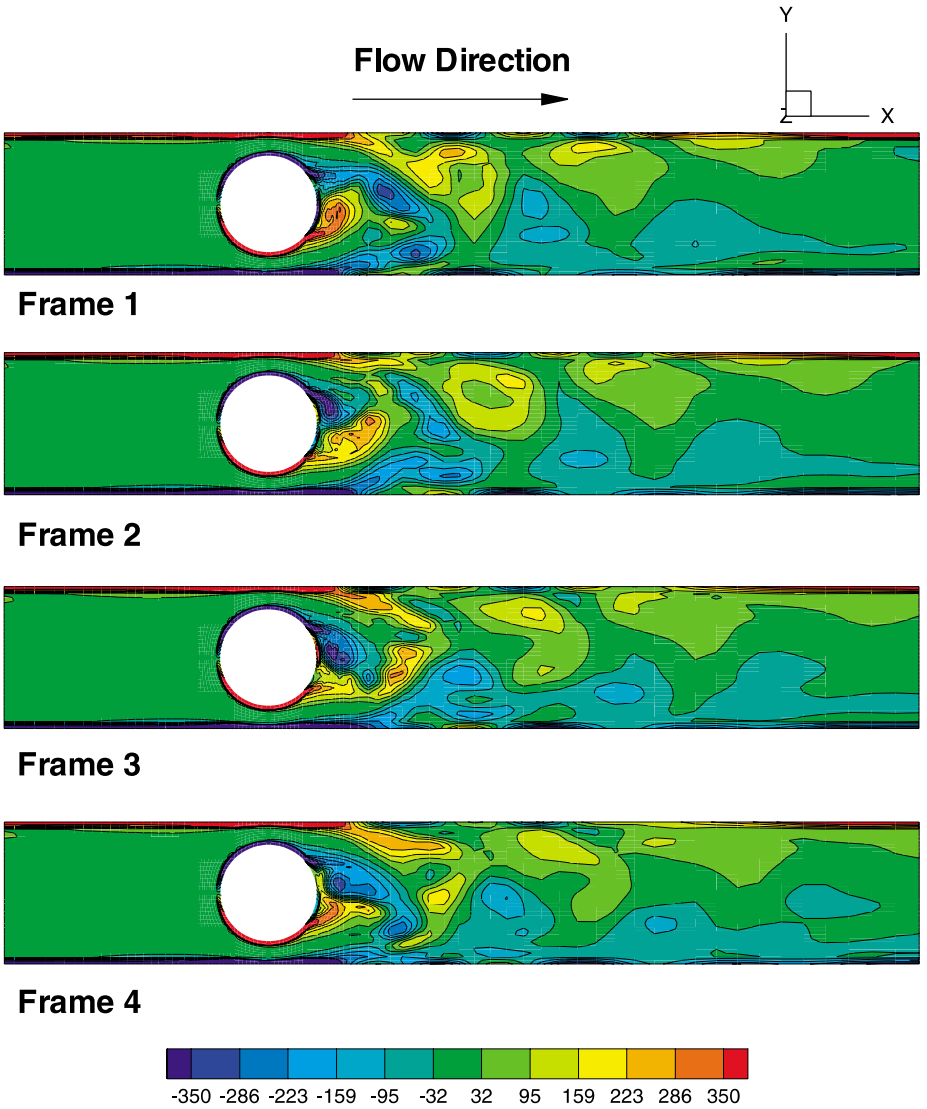

Fig. 18. Z-vorticity contours of single tube in a channel for four sequential frames.

the mean and turbulent stresses at the midplane $x/D = 0.65$. The V-shape profile of the mean velocity inside the recirculation zone has been described in experiments and captured in our simulation (Fig. 21(b)). The rms and Reynolds stress values are shown in Fig. 21(c) and (d), respectively. The profiles are similar to experimental data available for lower velocity simulations.

The GUSTCC computer program uses a central differencing scheme for its spatial discretization. It has been shown recently by Kravchenko and Moin [16] that LES calculations with central differencing schemes are in better agreement with experimental data than those performed with dissipative methods [16]. Breuer and Pourquie [3] have also shown that the influence of SGS model was not found to be strong when comparing between the Smagorinsky and dynamic SGS models. This agrees with lid-driven cavity results. No practical differences of the mean and stress values were seen between the two SGS models.

In order to perform some sensitivity studies of the GUSTCC computer program, parameter variations were studied. To assess the effect of the SGS model, we performed simulations with and without the SGS closure model. The simulation without the SGS model did not converge. From this we may conclude that for this Reynolds number with the given grid resolution, the SGS model contribution is significant to the flow and

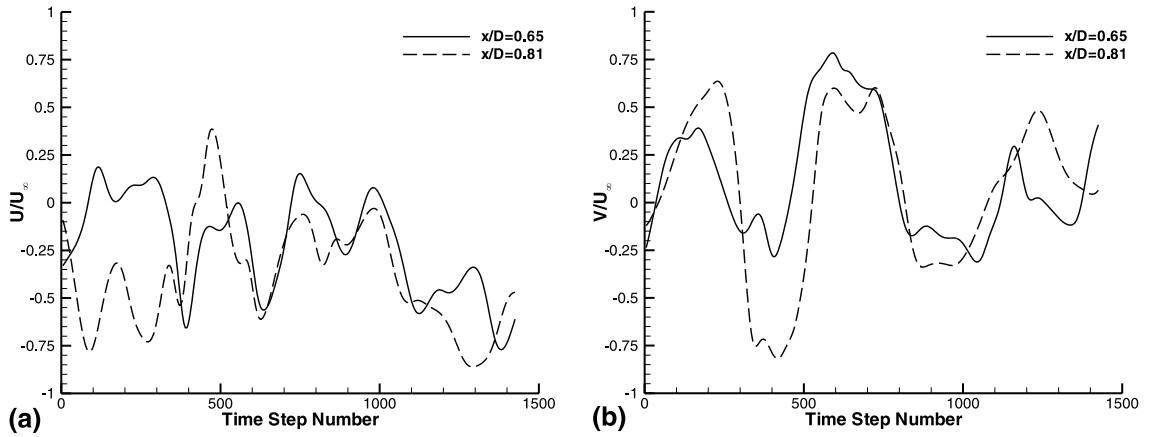

Fig. 19. Instantaneous (a) streamwise and (b) transverse values at midplane centerline $x/D = 0.65, 0.81$.

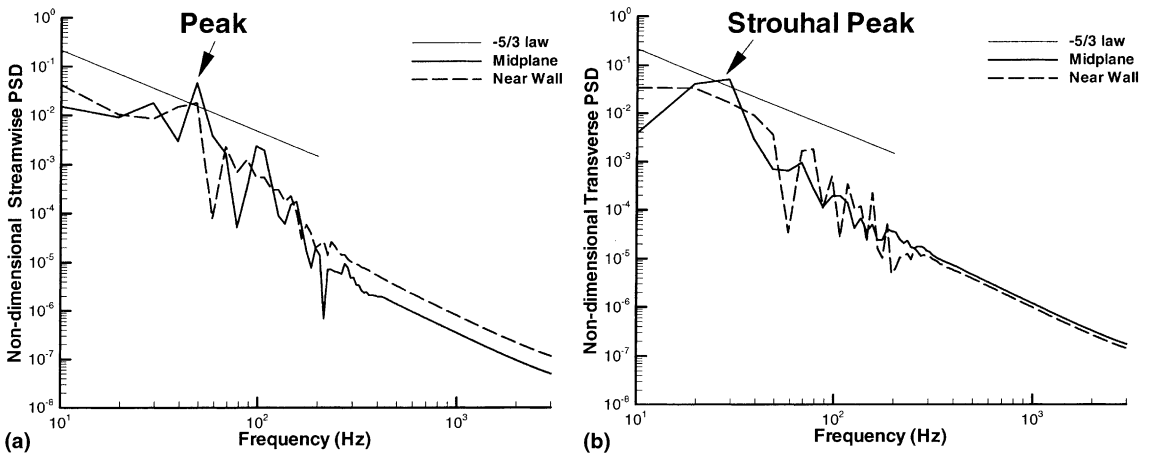

Fig. 20. Non-dimensional (a) streamwise, (b) transverse PSD at midplane and near wall for $x/D = 0.65$.

therefore cannot be ignored. Also, it shows that numerical diffusion is minimal.

To show that the resolution of the grid was adequate, a coarser mesh ($78 \times 34 \times 20$) was simulated with similar geometry and boundary conditions (with the exception of tube downstream length of $4D$ instead of $6D$). Considering the mean and statistical values, both cases compare well to each other. However, the wavelike structures and recirculation zones near the channel walls were not captured with the coarser mesh. A limiting factor in this case was the tube downstream length. It is recommended that longer regions be used. The wavelength of the streamwise structures in the near wake of a circular cylinder scale [34]

$$\frac{\lambda_z}{D} \sim 25 Re_{\mathrm{D}}^{-0.5}, \tag{28}$$

which is an estimate of the required spanwise resolution and domain size. The 32 cells in this direction satisfy that requirement.

Another test was performed to show if any unacceptable numerical damping was present. In the simulations without a SGS model, the time step was halved twice and applied to the simulation without a SGS model to see if numerical diffusion would cause the flow to converge. No such convergence was seen.

With the above simulation, the computer program was applied to complex geometries and captured experimentally observed physical phenomenon. The profiles of mean and statistical quantities are acceptable. The PSD plots are consistent with the instantaneous values. It is important to understand the flow dynamics of the wake of a bluff body and be able to predict the forces acting on that body. With the above

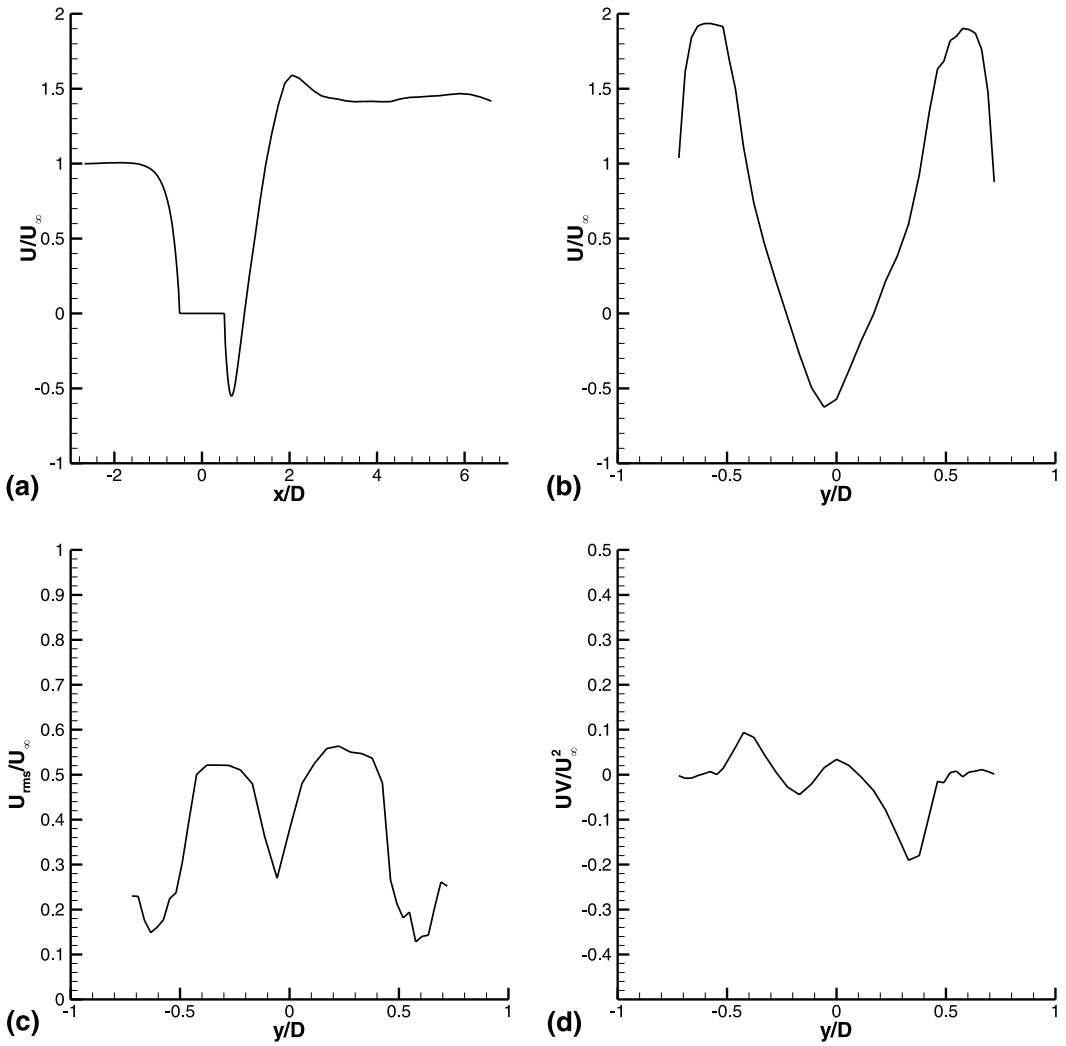

Fig. 21. Mean and stress profiles for single tube in a channel.

simulation, the vortex shedding behind the cylinder was captured.

11. Conclusions

The numerical prediction of turbulent flows for complex geometries was achieved using the large eddy simulation technique. In order to stabilize the variation of the model coefficient in the dynamic subgrid scale model, temporal and spatial low-pass filters were applied. Furthermore, upper and lower limits on the eddy viscosity were placed. The modifications improve the behavior of the dynamic subgrid scale model for the near-wall regions, in laminar flows and account for energy backscatter.

The new-wall model developed for complex geometries was based on the 1/7 power law. Shear stresses at the wall were evaluated in each direction. Ejection and sweep effects were added. These effect the shear stress near the wall. The velocity correlation with the shear stress was shifted in the downstream direction.

Results were validated in a lid-driven cavity flow. The complex separation and recirculation regions of this three-dimensional flow were used to validate the wall and subgrid scale models. Several wall models were tested. These compared well to experimental data. Taylor–Gortler-like and lower corner vortices were captured and visualization showed acceptable behavior of the flow. There was no significant difference between the dynamic subgrid scale and Smagorinsky closure models.

A simplified bluff body simulation with a single tube in a channel showed the capability of the computer program to capture unsteady phenomena. Visualization delineated the vortex shedding behind a circular cylinder as well as the effect of the channel walls. The complex structures reinforced the importance of three-dimensionality of the flow. Mean quantities agreed with expected profiles behind a circular cylinder. A weak form of the Strouhal peak was captured in the transverse velocity PSD. A peak at twice the Strouhal frequency was observed in the streamwise PSD.

The large eddy simulation computer program with subgrid scale model improvements and introduction of new-wall model was used. The results showed that the computer program was capable of unsteady flow simulation in complex geometry.

References

[1] E. Balaras, Finite-difference computations of high Reynolds number flows using the dynamic subgrid-scale model, Theoret. Comput. Fluid Dyn. 7 (1995) 207–218.

[2] E. Balaras, C. Benocci, Large eddy simulation of flow in a square duct, in: Proceedings of the 13th Symposium on Turbulence, Rolla, MO, 1992, pp. A33.1–A33.7.

[3] M. Breuer, M. Pourquie, First experiences with LES of flows past bluff bodies, in: W. Rodi, G. Bergeles (Eds.), in: Engineering Turbulence Modelling and Experiments 3, Elsevier, Netherlands, 1996, pp. 177–186.

[4] M. Breuer, W. Rodi, Large-eddy simulation of turbulent flow through a straight square duct and a bend, in: P.R. Voke et al. (Eds.), Direct and Large Eddy Simulation I, Kluwer Academic Publishers, Netherlands, 1994, pp. 273–285.

[5] P.J. Dionne, N. Vaida, GUSTCC: A Large Eddy Simulation Computer Code for Steam Generator Applications, Volume II: Programmers Manual, CFDRC Report 4038/1, CFD Research Corporation, Huntsville, AL, 1995.

[6] C.J. Freitas, R.L. Street, Non-linear transient phenomena in a complex recirculating flow: a numerical investigation, Int. J. Numer. Meth. Fluids 8 (1988) 769–802.

[7] C.J. Freitas, R.L. Street, A.N. Findikakis, J.R. Koseff, Numerical simulation of three-dimensional flow in a cavity, Int. J. Numer. Meth. Fluids 5 (1985) 561–575.

[8] M. Germano, U. Piomelli, P. Moin, W.H. Cabot, A dynamic subgrid-scale eddy viscosity model, Phys. Fluids A 3 (7) (1991) 1760–1765.

[9] S. Ghosal, T. Lund, P. Moin, A Dynamic Localization Model for Large-Eddy Simulation of Turbulent Flows, Annual Research Briefs, Center for Turbulence Research, Stanford, CA, 1993.

[10] G. Grotzbach, Direct numerical and large eddy simulation of turbulent channel flows, in: N.P. Cheremisionoff (Ed.), in: Encyclopedia of Fluid Mechanics VI, Gulf Publications, Houston, TX, 1987, pp. 1337–1391.

[11] F.R. Hama, Three-dimensional vortex pattern behind a circular cylinder, J. Aeronaut. Sci. 24 (1957) 156–158.

[12] S.A. Jordan, S.A. Ragab, A large-eddy simulation of the shear-driven cavity flow using dynamic modeling, Comput. Fluid Dyn. 6 (1996) 321–335.

[13] S.J. Kline, W.C. Reynolds, F.A. Schraub, P.W. Runstadler, The structure of turbulent boundary layers, J. Fluid Mech. 30 (1967) 733–741.

[14] J.R. Koseff, R.L. Street, The lid-driven cavity flow: a synthesis of qualitative and quantitative observations, ASME J. Fluids Eng. 106 (1984a) 390–398.

[15] J.R. Koseff, R.L. Street, Visualization studies of shear driven three-dimensional recirculating flow, ASME J. Fluids Eng. 106 (1984b) 21–29.

[16] A.G. Kravchenko, P. Moin, Numerical studies of flow over a circular cylinder at $Re_D = 3900$, Phys. Fluids A 12 (2) (2000) 403–417.

[17] S. Lee, A.K. Runchal, J.-O. Han, Subgrid-scale modeling in large-eddy simulation and its application to flow about yawed cylinder and cavity flows, in: Third ASME/JSME Joint Fluids Engineering Conference, San Francisco, CA, CD-ROM, 1999.

[18] A. Leonard, Energy cascade in large-eddy simulations of turbulent fluid flows, Adv. Geophys. A 18 (1974) 237–248.

[19] D.K. Lilly, A proposed modification of the germano subgrid-scale closure method, Phys. Fluids A 4 (3) (1992) 633–635.

[20] S. Liu, C. Meneveau, J. Katz, On the properties of similarity subgrid-scale models as deduced from measurements in turbulent jet, J. Fluid Mech. 275 (1994) 83–119.

[21] T.S. Lund, S. Ghosal, P. Moin, Numerical experiments with highly-variable eddy viscosity models, in: U. Piomelli, S.A. Ragab (Eds.), in: Engineering Application to Large Eddy Simulation, Springer, Berlin, 1993, pp. 7–11.

[22] C. Meneveau, T. Lund, W. Cabot, A Lagrangian dynamic subgrid-scale model of turbulence, J. Fluid Mech. 315 (1996) 353–385.

[23] S.V. Patankar, Numerical Heat Transfer and Fluid Flow, Hemisphere, New York, 1980.

[24] U. Piomelli, Large Eddy Simulation of Turbulent Flows, Theoretical and Applied Mathematics, TAM Report No. 767 (UILU-ENG-94-6023), University of Illinois, Urbana-Champaign, Urbana, IL, 1994.

[25] U. Piomelli, J. Ferziger, P. Moin, New approximate boundary conditions for large eddy simulations of wall-bounded flows, Phys. Fluids A 1 (6) (1989) 1061–1068.

[26] A.K. Prasad, J.R. Koseff, Reynolds number and end-wall effects in a lid-driven cavity flow, Phys. Fluids A 1 (2) (1989) 208–218.

[27] W. Rodi, Large-eddy simulations of the flow past bluff bodies: state-of-the art, JSME Int. J. Ser. B 41 (2) (1998) 361–373.

[28] A. Roshko, On the wake and drag of bluff bodies, J. Aeronaut. Sci. 22 (1955) 124–129.

[29] N.D. Sandham, A model equation for transitional and turbulent plane channel flow, in: U. Schumann, et al. (Eds.), Turbulent Shear Flows 8, Springer, Berlin, 1991, pp. 67–80.

[30] U. Schumann, Subgrid scale model for finite difference simulation of turbulent flows in plane channels and annuli, J. Comput. Phys. 18 (1975) 376–404.

[31] J. Smagorinsky, General circulation experiments with primitive equations, Monthly Weather Rev. 91 (1963) 216–241.
[32] H. Tennekes, J.L. Lumley, A First Course in Turbulence, MIT Press, Cambridge, MA, 1972.
[33] H. Werner, H. Wengle, Large-eddy simulation of turbulent flow over and around a cube in a plate channel, in: U. Schumann, et al. (Eds.), Turbulent Shear Flows 8, Springer, Berlin, 1991, pp. 155–168.
[34] C.H.K. Williamson, Vortex dynamics in the cylinder wake, Ann. Rev. Fluid Mech. 28 (1996) 477–539.
[35] Y. Zang, R.L. Street, J.R. Koseff, A dynamic mixed subgrid-scale model and its application to turbulent recirculating flows, Phys. Fluids A 5 (12) (1993) 3186–3196.